JOURNAL OF SPACECRAFT AND ROCKETS
Vol. 32, No. 3, May–June 1995

Unsteady Flowfield over a Forward-Looking Endoatmospheric Hit-to-Kill Interceptor

H. Q. Yang*
CFD Research Corporation, Huntsville, Alabama 35805
and
Mark Antonison†
BDM Engineering Services Company, Huntsville, Alabama 35806

A forward-looking recessed aperture interceptor has significant aero-optical and aerothermal advantages. Previous experimental studies have shown that the flowfield in front of a forward-looking cavity is unsteady, and the bow shock oscillates at the cavity fundamental resonant frequency. In this study, an advanced computational fluid dynamics code is applied to study the aforementioned unsteady phenomena. The code is first validated against the experiments and good comparisons are found. The numerical parametric study shows that the existence of an oscillatory bow shock is very sensitive to the cavity geometry. At a field of view (FOV) of 60 deg, the initial transient quickly dampens out to a steady state. With a decrease of FOV, an unsteady oscillatory flowfield is sustained after the initial transient, and the amplitude of oscillation is a function of FOV. For an FOV of 20 deg, the amplitude of pressure oscillation is 25% of the mean value in the cavity. For an FOV of 10 deg, it can be as high as 50%.

Nomenclature

E, F, H	= numerical fluxes
e	= internal energy per unit mass
e_t	= total enthalpy per unit mass
M	= Mach number
P_t	= total pressure at the center of a concave nose cavity
p	= pressure
$\boldsymbol{Q}$	= conservative variable vector
s	= distance along the cavity wall
s_1	= cavity arc length
u, v	= velocity component in x and y directions, respectively
x	= axial coordinate
y	= radial coordinate
ξ, η	= curvilinear coordinates
ρ	= density
$\Psi(r)$	= limiter function with r as monitor

Subscripts

i, j	= at control volume center
$i+1/2, j+1/2$	= at control volume faces

Superscripts

L, H	= low- and high-order schemes

Introduction

UNLIKE the conventional side-looking interceptor, the seeker window in this study is mounted at the base of a forward-looking cavity recessed in the front end of the interceptor, as shown in Fig. 1. The challenge addressed by this design is to allow the seeker to "see where it is going" well enough to achieve a direct hit when "homing" in the atmosphere at hypersonic velocity. The purpose of the present hit-to-kill endoatmospheric strapdown seeker (HESS) program is to assess the aero-optical and aerothermal performance of the forward-looking interceptor. A previous program, the hollow-nosed active seeker program (HASP)[1] showed that a nearly normal bow shock will exist in front of the forward-looking cavity; reduced seeker window heating at the base of the cavity can be achieved, even at high Mach numbers (i.e., $M = 10$); a near constant density gas flowfield exists in the cavity; and for a 10 deg field of view (FOV) cavity (see Fig. 1) an unsteady flowfield develops in front of the vehicle forebody wherein the bow shock oscillates at the cavity fundamental resonant frequency.

The performance of an optical seeker is dependent on the refractive and radiative environment produced by the hypersonic flowfield and bow shock. The principal aero-optical effect of an oscillating bow shock is a time-varying defocus of the target image on the seeker focal plane array. At off-axis look angles, a time-varying component of boresight error will, thus, be introduced. These effects are complex and difficult to evaluate analytically, and it is particularly challenging to develop design solutions that will minimize the impact of these effects on seeker performance. Elimination of the bow-shock oscillation is preferred; a reduction of the amplitude of bow-shock motion and an increase in frequency to levels that can be filtered are also required.

Periodic shock motions in front of a concave cylinder cavity have been observed experimentally for more than three decades.[2–4] This phenomenon has also been found in supersonic parachutes where a shock wave moves back and forth ahead of the canopy, affecting the inflation stability. Stallings and Burbank[2] measured heat transfer coefficients and local pressures on a 5.46-in.-diam. cylinder with a concave nose for a Mach number range of 2.49 to 4.44, Reynolds number range from 0.94×10^6 to 2.16×10^6, and angle-of-attack range from 0 to 15 deg. They found two types of flow phenomena associated with the measurement: a steady flowfield and an unsteady flowfield similar to inlet buzzing. The unsteady flow was found to be unpredictable and sporadic, and it became predominant at small angles of attack and higher Mach numbers.

Bastianon[3] attempted to explain the aerodynamic instability around a concave body immersed in a supersonic freestream by numerical computation of axisymmetric inviscid flow over a nonporous cavity. He found that when the cavity depth exceeded a given limit, a periodic solution was predicted that corresponded to experimental observations.

Bohachevsky and Kostoff[4] employed a first-order accurate numerical method of unsteady adjustment to calculate inviscid flowfields about convex and concave shapes. The concave bodies are

Presented as Paper 93-0501 at the AIAA 31st Aerospace Sciences Meeting, Reno, NV, Jan. 11–14, 1993; received Feb. 16, 1993; revision received Sept. 27, 1993; accepted for publication Oct. 6, 1993.

*Group Leader/Research. Member AIAA.
†Engineer.

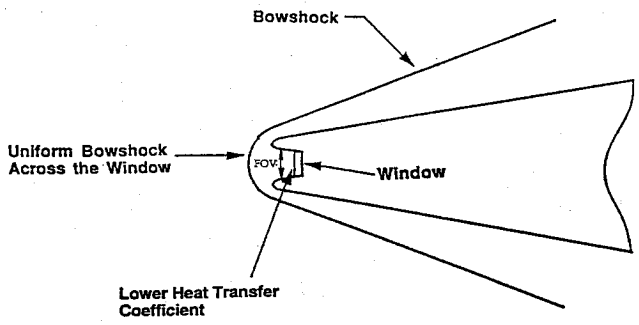

Fig. 1 Schematic of recessed aperture seeker system.

thin-walled cylinders with cylindrical cavities of different depths facing the oncoming stream. The calculations showed that flows relaxed to their steady state in a damped oscillatory manner. They suggested that high-order accurate computations were necessary to resolve the nature of these oscillations.

The objective of this paper is to explain the unsteady behavior of the bow shock in front of a forward-looking cavity by numerical computation of transient compressible flow over the recessed aperture cavity and to study the transient movement (oscillation) of the bow shock and its effect on optical aberration. The influence of cavity geometry and its implication to the recessed aperture cavity design will be analyzed.

Theoretical Formulation

The model under consideration is shown in Fig. 1. It is a concave nose cavity immersed in a supersonic flow. Under the zero angle-of-attack condition and inviscid assumption, the two-dimensional axisymmetric Euler equations were used to describe the flow motion:

$$\frac{\partial \boldsymbol{Q}}{\partial t} + \frac{\partial E}{\partial x} + \frac{\partial F}{\partial y} + H = 0 \tag{1}$$

where

$$\boldsymbol{Q} = \begin{Bmatrix} \rho \\ \rho u \\ \rho v \\ \rho e_t \end{Bmatrix}, \quad E = \begin{Bmatrix} \rho u \\ \rho u^2 + p \\ \rho uv \\ \rho(e_t + p)u \end{Bmatrix}$$

$$\{F\} = \begin{Bmatrix} \rho v \\ \rho uv \\ \rho v^2 + p \\ \rho(e_t + p)v \end{Bmatrix}, \quad H = \frac{1}{y}\begin{Bmatrix} \rho u \\ \rho vu \\ \rho v^2 \\ \rho(e_t + p)v \end{Bmatrix} \tag{2}$$

$$e_t = e + \tfrac{1}{2}(u^2 + v^2) \tag{3}$$

Definitions of all variables can be found in the nomenclature section.

Equation (3) can be transformed from Cartesian polar coordinates x, y to curvilinear coordinates ξ, η as

$$\frac{\partial \tilde{\boldsymbol{Q}}}{\partial t} + \frac{\partial \tilde{E}}{\partial \xi} + \frac{\partial \tilde{F}}{\partial \eta} + \tilde{H} = 0 \tag{4}$$

where

$$\begin{aligned} \tilde{\boldsymbol{Q}} &= (\boldsymbol{Q}/J) \\ \tilde{E} &= (1/J)(\xi_x E + \xi_y F) \\ \tilde{F} &= (1/J)(\eta_x E + \eta_y F) \\ \tilde{H} &= (H/J) \end{aligned} \tag{5}$$

FASTRAN, a time-accurate computational fluid dynamics (CFD) code, was used to perform the CFD computations. The FASTRAN code is a multidimensional (two- and three-dimensional), explicit/implicit, density-based, finite volume Navier–Stokes solver for compressible flows. In the FASTRAN code, Eq. (4) is discretized by integration over a control volume $\Delta\eta\Delta\xi$ as

$$(1/\Delta t)[(\tilde{\boldsymbol{Q}}^{n+1} - \tilde{\boldsymbol{Q}}^{n})\Delta\eta\Delta\xi]_{i,j} + (\tilde{E}\Delta\eta)_{i+\frac{1}{2},j} - (\tilde{E}\Delta\eta)_{i-\frac{1}{2},j}$$

$$+ (\tilde{F}\Delta\xi)_{i,j+\frac{1}{2}} - (\tilde{F}\Delta\xi)_{i,j-\frac{1}{2}} + (\tilde{H}\Delta\eta\Delta\xi)_{i,j} = 0 \tag{6}$$

The solution of this equation depends on the way the cell face fluxes $\tilde{E}_{i+1/2,j}$, $\tilde{F}_{i,j+1/2}$ are calculated. Currently, a hybrid scheme of the form

$$\tilde{E}_{i+\frac{1}{2},j} = \tilde{E}^{L}_{i+\frac{1}{2},j} + \Psi(r)\left(\tilde{E}^{H}_{i+\frac{1}{2},j} - \tilde{E}^{L}_{i+\frac{1}{2},j}\right) \tag{7}$$

is employed. The evaluation of $\tilde{E}^{L}_{i+1/2,j}$ involves approximate solution to a Riemann problem with given left and right states $(\boldsymbol{Q}_{i+1,j}, \boldsymbol{Q}_{i,j})$. The FASTRAN code is composed of modules that allow the user to choose from several approximate Riemann solvers: Roe's flux difference splitting,[5] van Leer's flux vector splitting,[6] Stegger–Warming's flux vector splitting,[7] and Godunov's approximate solver.[8] The evaluation of $\tilde{E}^{H}_{i+1/2,j}$ ranges from second-order up to fourth-order accuracies. Use of the limiter $\psi(r)$ ensures satisfaction of the total variation diminishing (TVD) property of the flux in each individual direction. The user can select various advanced differencing schemes, from Roe–Sweby's TVD,[9–11] Yee's TVD,[12] Chakravarthy and Osher's TVD,[13] to Colella and Glaz's PLM.[14]

The FASTRAN code can also accommodate a variety of boundary conditions, including inflow, outflow, solid wall, symmetry plane, and periodic boundaries. For high-speed flows, FASTRAN can take high temperature and chemical equilibrium conditions into account by adopting an "equivalent" γ representation, as proposed by Grossman and Walters.[15]

Results and Discussion

Validation

FASTRAN has been validated in over more than 20 cases, including transient and steady-state problems, and good agreement with experimental data, theoretical solutions, and other published results have been shown.[16–19] In the ensuing discussion, only the most related experimental data and validation are presented.

The model of the problem is taken from the work of Stallings and Burbank[2] and is shown in Fig. 2a. The geometry is a concave nose cylinder, and dimensions in the figure are in inches. The outside radius of the lip is 0.1 in. A mesh of 100 × 60 is generated around the cylinder by an elliptic grid generator, as shown in Fig. 2b. The

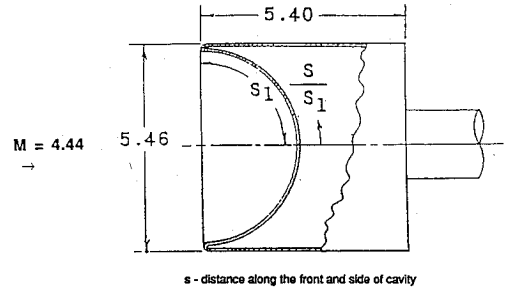

a) Experimental model

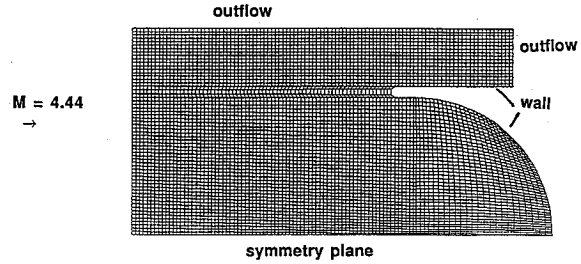

b) Computational grid and boundary conditions

Fig. 2 Experimental and computational model for a concave nose cylinder in a supersonic stream of Mach number 4.44.

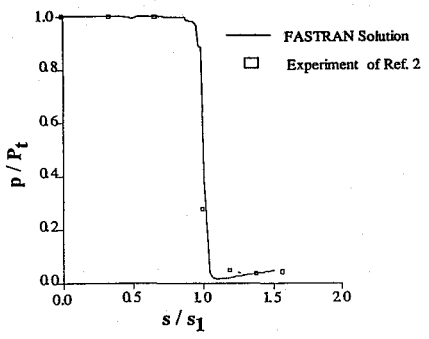

a) Pressure distribution over the front face and side

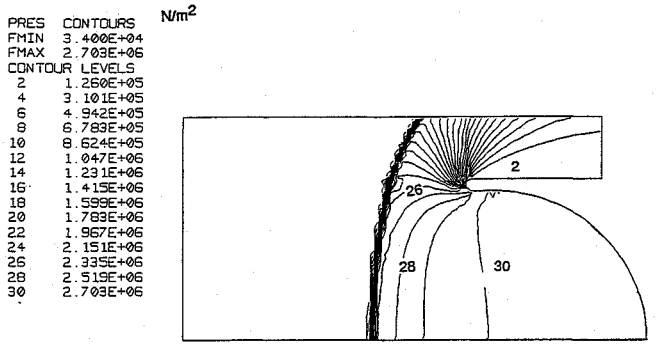

b) Pressure contours

Fig. 3 Predicted flowfield of Mach 4.44 flow over a concave nose cylinder.

boundary conditions are also specified. The inflow properties are ambient temperature and pressure ($T = 300\,\text{K}$, $p = 1.0\times10^5\,\text{N/m}^2$) with Mach number 4.44, and the initial condition is quiescent flow with ambient temperature and pressure.

The computation was made with van Leer's flux vector splitting as the Riemann solver in Eq. (7) and minimode limiter for high-order differencing. This will ensure essentially second-order accuracy in time and space over most of the computational domain, except near the shock wave. It was found that the initial transient quickly damped out and a steady state was reached in a short period of time for this condition.

Fig. 3a displays a comparison of experimental measurements[2] and the FASTRAN prediction for the pressure distributions over the front face and sides of the concave nose cylinder. The agreement is fairly good. P is the total pressure at the center of the concave nose cavity, and the definition of s/s_1 is shown in Fig. 2a. The corresponding pressure field is given in Fig. 3b. As observed in the experiment,[2] the predicted local pressure from the stagnation point of the concave nose to approximately 80% of nose cavity surface length is the same as the total pressure behind the normal shock.

Initial Transient for Baseline HESS Design

The initial transient corresponds to the short time (≈30 ms) after shroud removal during the interceptor operation. In the reported results, the air is assumed to be inviscid and at chemical equilibrium. The inviscid assumption in this study removed the requirement of grid clustering near the wall, and hence significantly increased the time-step size for the transient calculation. A 120 × 50 grid for the baseline model of HESS (Fig. 1) is shown in Fig. 4, along with boundary conditions. The freestream Mach number is 6.6. The baseline HESS window has a 60 deg FOV. A sharp discontinuity was prescribed, as shown by the left and right states in the figure.

Figure 5 shows pressure–time history at the cavity window base. The pressure spike is caused by the impingement of the shock front on the window. The bow shock motion is implied by the pressure oscillation at the wall. Unlike the pressure oscillation in the previous HASP program, the pressure oscillation damps out very quickly for the baseline HESS configuration.

The results for a viscous calculation is also shown in Fig. 5, to investigate the effect of viscosity on the flowfield solution. It is seen

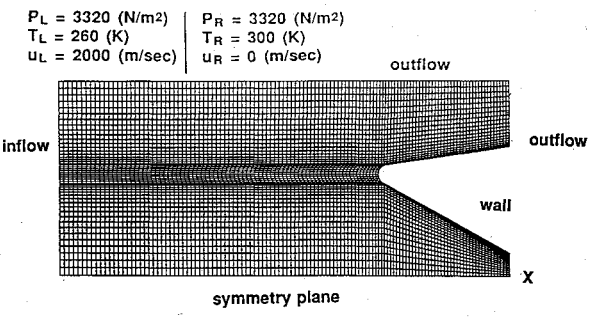

Fig. 4 Baseline HESS design and computational model.

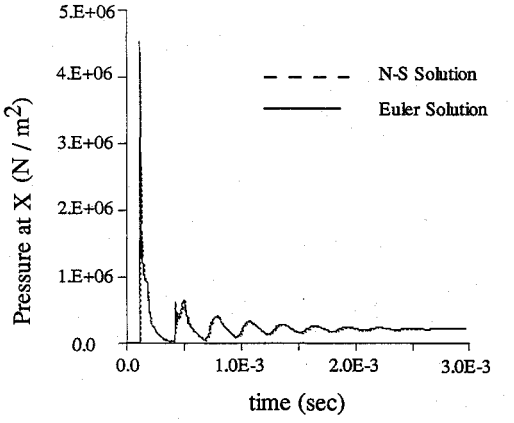

Fig. 5 Pressure history at cavity window base for baseline HESS design, $M = 6.6$.

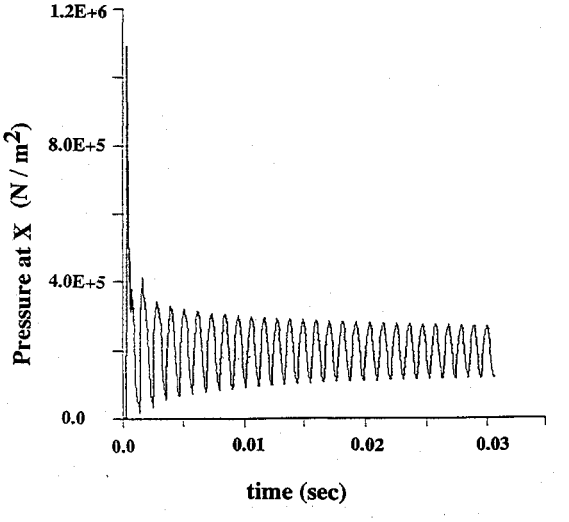

Fig. 6 Pressure history at cavity center for HASP geometry at HESS flight condition, $M = 6.6$.

that the pressure–time histories with and without viscosity effects are essentially the same.

Evaluation of HASP Design

To understand why the pressure oscillation damped, the HASP design was revisited. As mentioned in the introduction, the HASP design produced an unsteady flowfield in front of the vehicle forebody at $M = 10$. The unsteady flow was likewise predicted by FASTRAN for $M = 10$ (results not shown). To eliminate the possibility of flow conditions causing the shock oscillation, the HASP model was run at the same flow conditions as the HESS model, $M = 6.6$. The FOV is now 10 deg. As indicated in Fig. 6, a periodic pressure oscillation is detected at the center of the cavity, and the amplitude is almost constant. This implies the oscillatory motion of the bow shock.

Table 1 Effect of field of view on the unsteady flowfield

FOV, deg	Flow character	Oscillatory pressure amplitude,%	Oscillatory frequency, Hz
60	Steady	0	0
40	Unsteady	2%	2777
20	Unsteady	25%	1548
10	Unsteady	50%	925

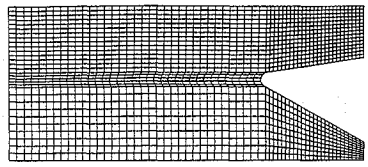

a) FOV of 60 deg

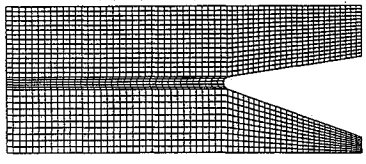

b) FOV of 40 deg

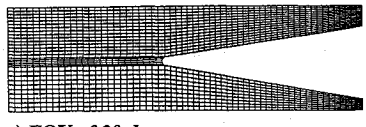

c) FOV of 20 deg

Fig. 7 Computational geometries.

Effect of Field of View on the Unsteady Flowfield

One variable that changes substantially between the HASP and HESS configurations is FOV. The HASP configuration had a FOV of 10 deg, whereas the baseline HESS configuration had a FOV of 60 deg. To determine the effect of FOV on shock oscillation, parametric computations were made with FOV varying from 60 to 20 deg. The cavity geometry was modified so that the cavity rim diameter and aperture diameter were maintained constant, and the cavity depth was systematically varied.

The computational grids are shown in Fig. 7 for each FOV. The predicted pressure at the cavity wall, indicated in Fig. 8, clearly shows the impact of geometric configuration on the steadiness of the flowfield. At a FOV of 60 deg (Fig. 8a), the initial pressure spike, caused by the removal of the shroud, decays very quickly. A steady state is reached in a few milliseconds (4.3×10^{-3} s). When the FOV is decreased to 40 deg (Fig. 8b), the acoustic oscillation dampens out, but a steady state (i.e., no oscillation) is not attained. As indicated in Fig. 8b by the pressure traces, a relatively small oscillatory amplitude is preserved. At a FOV of 20 deg (Fig. 8c) the initial transient is predicted to be a highly unsteady, oscillatory flowfield. The frequency of the oscillation is found to be the same as the acoustic frequency in the cavity, based on a length scale that is the cavity depth and an acoustic speed at stagnation temperature. The amplitude of the pressure oscillation is 25% of the total pressure in the cavity. For the HASP design, the oscillatory amplitude (Fig. 6) was about 50% of the total pressure in the cavity. It can be concluded that the occurrence of an unsteady flowfield is very sensitive to the geometry; a periodic bow shock motion is likely to occur at low FOV, and the amplitude of the oscillation will increase with a decrease in FOV. Physically, the lateral walls of the cavity play a significant role in the bow-shock motion. At high FOV, the scattering effect of continuous reflections of acoustic waves at the lateral walls tends to dissipate the acoustic energy, and hence it causes rapid decay of the pressure oscillations. Table 1 summarizes the findings of this parametric study.

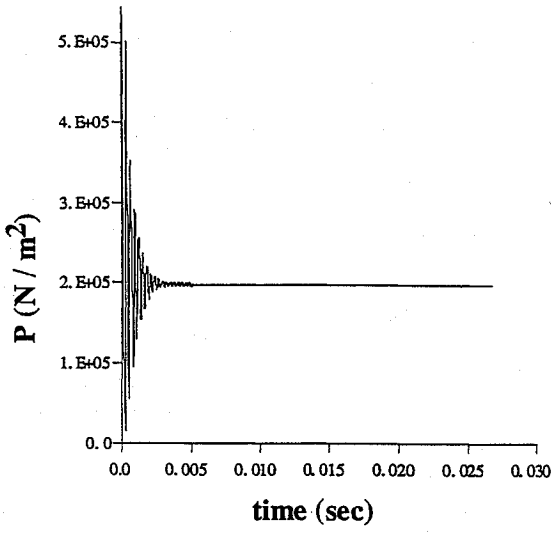

a) FOV of 60 deg

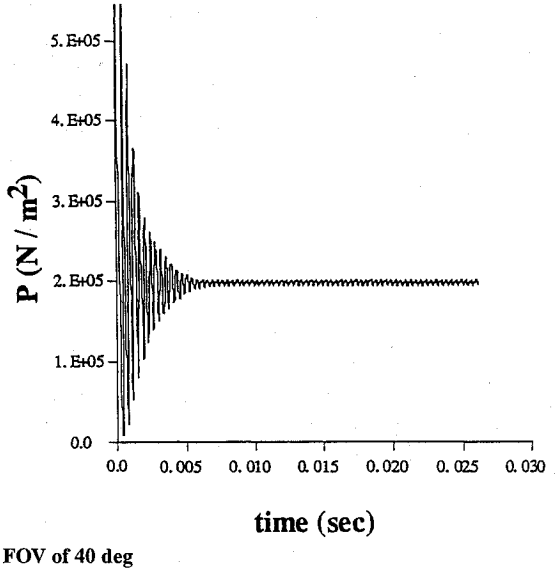

b) FOV of 40 deg

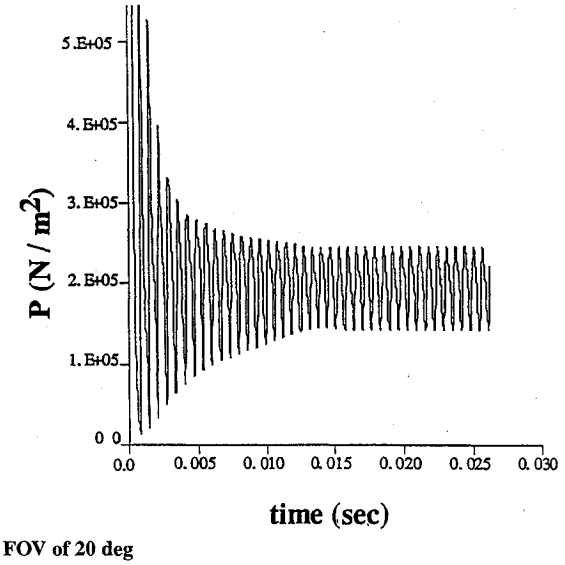

c) FOV of 20 deg

Fig. 8 Pressure-time history at recessed aperture window base.

Conclusions

A numerical study was conducted to investigate the oscillatory bow-shock behavior observed experimentally in front of concave nose cavities in hypersonic flow. A time-accurate, multidimensional, density-based Navier–Stokes code, FASTRAN, was used with an inviscid assumption to simulate the initial transient (i.e., immediately after shroud removal exposing the nose cone) over several HESS recessed aperture cavity designs. The numerical calculations indicated that the existence of oscillatory bow-shock motion is very sensitive to the cavity geometry. At a FOV of 60 deg, which is the baseline design for the HESS program, the initial transient, quickly dampened out to a steady state. With a decrease of FOV, an unsteady oscillatory flowfield was sustained after an initial transient, and the amplitude of the oscillation is a function of FOV. For a FOV of 20 deg, the amplitude of pressure fluctuation was 25% of the mean value in the cavity. For a FOV of 10 deg, it can be as high as 50%.

The prediction methodology demonstrated in this investigation will aid the design of missiles with a forward-facing nose cavity. In addition, this methodology will be useful in determining an appropriate sensor frequency bandwidth in an aerothermodynamic experiment and in assessing aero-optical effects.

Acknowledgments

The authors thank C. E. Smith, A. J. Przekwas, and A. K. Singhal of CFD Research Corporation for many constructive and insightful discussions during the course of this study, and J. Swann for preparation of the manuscript. The FASTRAN code used in this study was developed by CFD Research Corporation under the NASA Marshall Space Flight Center SBIR Project NAS8-38034.

References

[1]Marquart, E. J., and Grubb, J. P., "Investigation of the Flow Dynamics of a Forward-Facing Nose Cavity at Mach 10," Arnold Engineering Development Center, AEDC-TMR-86-V56, Arnold AFB,1987.

[2]Stallings, R. L., and Burbank, P. B., "Heat Transfer and Pressure Measurements on a Concave-Nose Cylinder for a Mach Number Range of 2.09 to 4.44," NASA TM-X-221, 1959.

[3]Bastianon, R., "Steady and Unsteady Solution of the Flowfield over Concave Bodies in Supersonic Free Stream," AIAA Paper 68-946, 1968.

[4]Bohachevsky, I. O, and Kostoff, R. N., "Supersonic Flow over Convex and Concave Shapes with Radiation and Ablation Effects," *AIAA Journal*, Vol. 10, No. 8, 1972, pp. 1024–1031.

[5]Roe, P. L., "Approximate Riemann Solvers, Parameter Vectors, and Difference Schemes," *Journal of Computational Physics*, Vol. 43, 1981, pp. 357–372.

[6]van Leer, B., "Upwind-Difference Methods for Aerodynamic Problems Governed by the Euler Equations," *Lectures in Applied Mathematics*, Vol. 22, American Mathematical Society, 1985, pp. 266–327.

[7]Stegger, J. L., and Warming, R. F., "Flux Vector Splitting of the Inviscid Gasdynamic Equations with Application to Finite Difference Methods," *Journal of Computational Physics*, Vol. 40, 1981, pp. 263–293.

[8]Godunov, S. K., "A Difference Method for the Numerical Calculation of Discontinuous Solutions of Hydrodynamic Equations," *Mat-Sbornik*, Vol. 47, 1959, pp. 357–393.

[9]Roe, P. L., "Characteristic-Based Schemes for the Euler Equations," *Annual Review of Fluid Mechanics*, 1986, pp. 337–356.

[10]Roe, P. L., "Some Contributions to the Modeling of Discontinuous Flows," *Lectures in Applied Mathematics*, Vol. 22, 1985, pp. 163–193.

[11]Sweby, P. K., "High Resolution Schemes Using Flux Limiters for Hyperbolic Conservation Laws," *SIAM Journal on Numerical Analysis*, Vol. 21, No. 5, 1984, pp. 995–1011.

[12]Yee, H. C., "A Class of High-Resolution Explicit and Implicit Shock-Capturing Methods," NASA TM-101088, 1989.

[13]Chakravarthy, S. R., and Osher, S., "A New Class of High-Accuracy TVD Schemes for Hyperbolic Conservation Laws," AIAA Paper 85-0363, 1985.

[14]Colella, P., and Glaz, H. M., "Efficient Solution Algorithms for the Riemann Problem for Real Gases," *Journal of Computational Physics*, Vol. 59, No. 2, 1985, pp. 264–289.

[15]Grossman, B., and Walters, R. W., "Analysis of Flux-Split Algorithms for Euler's Equation with Real Gases," *AIAA Journal*, Vol. 27, No. 5, 1989, pp. 524–531.

[16]Yang, H. Q., Pindera, M. Z., and Przekwas, A. J., "Assessment of Advanced Numerical Schemes for Multidimensional Fast Transient Compressible Flows with Moving Waves and Discontinuities," Ninth Annual CFD Workshop Group Meeting, NASA Marshall Space Flight Center, AL, April 1991.

[17]Pindera, M. Z., Yang, H. Q., Przekwas, A. J., and Tucker, K., "Assessment of Modern Methods of Numerical Simulations of High-Speed Flows," AIAA Paper 92-0052, 1992.

[18]Yang, H. Q., and Przekwas, A. J., "Prediction of Shock Pattern Dynamics at Hypersonic Angle of Attack Maneuvers of Endo-Kew Missile Forebodies," AIAA Paper 92-2768, 1992.

[19]Pindera, M. Z., Mo, G., Harrand, V. J., and Fickie, K., "Visualization and Analysis of Hypersonic Flows and Comparison to Experimental Data," AIAA Paper 92-2744, 1992.

G. T. Chrusciel
Associate Editor